

# Methane Decomposition and Carbon Growth on $\text{Y}_2\text{O}_3$ , Yttria-Stabilized Zirconia, and $\text{ZrO}_2$

Michaela Kogler,<sup>†</sup> Eva-Maria Köck,<sup>†</sup> Lukas Perfler,<sup>‡</sup> Thomas Bielz,<sup>†</sup> Michael Stöger-Pollach,<sup>§</sup> Walid Hetaba,<sup>§</sup> Marc Willinger,<sup>⊥</sup> Xing Huang,<sup>⊥</sup> Manfred Schuster,<sup>⊥</sup> Bernhard Klötzer,<sup>†</sup> and Simon Penner<sup>†,\*</sup>

<sup>†</sup>Institute of Physical Chemistry, University of Innsbruck, Innrain 52a, A-6020 Innsbruck, Austria

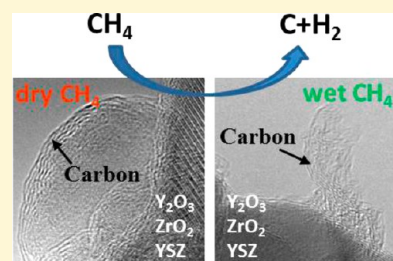
<sup>‡</sup>Institute of Mineralogy and Petrography, University of Innsbruck, Innrain 52f, A-6020 Innsbruck, Austria

<sup>§</sup>University Service Centre for Transmission Electron Microscopy (USTEM), Vienna, University of Technology, Wiedner Hauptstrasse 8-10/052, A-1040 Vienna, Austria

<sup>⊥</sup>Fritz-Haber-Institut der Max-Planck-Gesellschaft, Faradayweg 4-6, D-14195 Berlin, Germany

## S Supporting Information

**ABSTRACT:** Carbon deposition following thermal methane decomposition under dry and steam reforming conditions has been studied on yttria-stabilized zirconia (YSZ),  $\text{Y}_2\text{O}_3$ , and  $\text{ZrO}_2$  by a range of different chemical, structural, and spectroscopic characterization techniques, including aberration-corrected electron microscopy, Raman spectroscopy, electric impedance spectroscopy, and volumetric adsorption techniques. Concordantly, all experimental techniques reveal the formation of a conducting layer of disordered nanocrystalline graphite covering the individual grains of the respective pure oxides after treatment in dry methane at temperatures  $T \geq 1000$  K. In addition, treatment under moist methane conditions causes additional formation of carbon-nanotube-like architectures by partial detachment of the graphite layers. All experiments show that during carbon growth, no substantial reduction of any of the oxides takes place. Our results, therefore, indicate that these pure oxides can act as efficient nonmetallic substrates for methane-induced growth of different carbon species with potentially important implications regarding their use in solid oxide fuel cells. Moreover, by comparing the three oxides, we could elucidate differences in the methane reactivities of the respective SOFC-relevant purely oxidic surfaces under typical SOFC operation conditions without the presence of metallic constituents.



## 1. INTRODUCTION

Yttria-stabilized zirconia (YSZ) is used in a variety of technological applications, such as thermal barrier coatings or acting as a thermal insulating layer on superalloys in aircraft engines,<sup>1</sup> but is mostly used for high-temperature applications where efficient oxide ion transport is required. Hence, it is one of the most thoroughly investigated solid oxide ion conductor materials, mostly because of its high ionic conductivity linked with mechanical and chemical stability over a wide temperature and oxygen partial pressures range.<sup>2,3</sup> These properties make YSZ especially attractive for solid oxide fuel cell (SOFC) applications, either as an electrolyte or (combined with Ni) as anode material.<sup>2</sup> SOFC development and research has significantly increased in the past few years because of the need for efficient cogeneration of electrical power and heat from natural gas, thereby allowing for flexible fuel composition and low pollutant emission compared to other types of energy systems.<sup>4,5</sup> Of all components of a SOFC, the anode is most important in the oxidation of the fuel to generate electrons. It prevents concentration polarization through removal of reaction products through the anode substrate, and it provides suitable electrical conductivity to decrease ohmic polarization. Gas permeability and electrical conductivity of SOFC anodes

are strongly controlled by the microstructural parameters such as porosity, phase distribution, or particle size. Therefore, careful control of the microstructure is essential for the optimization of the electrochemical performance of an anode. One of the most frequently used anode materials for SOFCs is a double phase nickel and YSZ (Ni/YSZ) “cermet” material, where Ni is both regarded as a catalyst for the internal reforming of methane to  $\text{CO}/\text{H}_2$  and the subsequent electro-oxidation of hydrogen and CO to water and  $\text{CO}_2$ , whereas YSZ forms a porous ceramic network required to create an extended reaction zone as well as to adapt the thermomechanical properties of the anode to the ones of the other cell components.<sup>5–9</sup> In addition to hydrogen, several hydrocarbons, transforming to  $\text{H}_2$  and CO by external or internal reforming processes, can also be used as fuels.<sup>10</sup> Because of its abundance and high hydrogen-to-carbon ratio, methane as hydrogen/carbon source is regarded as the main energy source for fuel cell technology. Efficient internal reforming of methane in SOFCs is desirable, as it allows for less costly and complex systems,

Received: December 11, 2013

Revised: February 4, 2014

Published: February 5, 2014

with the additional advantage that the waste heat being released from the electrode can be utilized to drive the endothermal methane steam reforming reaction directly. Nevertheless, one of the most serious drawbacks upon using hydrocarbon-rich fuel gas is the deposition of carbon or carbon filament formation on the electrode, blocking gas diffusion at the catalytically active triple phase boundary anode/electrolyte/fuel by coking, and in parallel inducing mechanical damage via carbon filament formation and nickel “dusting”. This is a particularly important problem if Ni/YSZ anode systems are used because of the efficient methane dissociation and subsequent carbon incorporation of Ni-containing materials.<sup>11–14</sup> Although previously assumed to be a sole problem of complex anode systems, recent investigations on hydrocarbon dissociation on ZrO<sub>2</sub> materials revealed that even using pure oxidic materials, formation of different carbon architectures is possible. This research showed that nanoparticulate zirconia is able to catalyze the growth of single-walled and multiwalled carbon nanotubes (CNTs) under special CVD growth conditions.<sup>15</sup> In turn, this might have important implications also for fuel cell research because potential hydrocarbon dissociation and carbon deposition eventually also partially proceed via the pure oxidic ceramic network.

On the basis of these previous experiments, the goal of this work is to investigate the hydrocarbon dissociation and carbon deposition capability of the most common SOFC electrolyte material YSZ in comparison to its oxidic constituents ZrO<sub>2</sub> and Y<sub>2</sub>O<sub>3</sub>. Using methane as hydrocarbon source, this will eventually reveal if a set of experimental parameters exists that allows for efficient methane activation over oxidic materials under realistic operational conditions of an SOFC. Particular emphasis will also be given to the eventual formation of different carbon architectures. As over alumina-supported Fe catalysts, CNT growth has been suspected to be substantially influenced by water,<sup>16–21</sup> both dry methane conversion and experiments mimicking methane steam reforming conditions were performed in parallel, and consequently, all measurements were conducted under dry and moist conditions. To fulfill this task, a set of different structural and spectroscopic characterization methods were used, including aberration-corrected electron microscopy, Raman spectroscopy, electrochemical impedance spectroscopy, and volumetric adsorption techniques.

## 2. EXPERIMENTAL SECTION

**2.1. Materials.** Commercial powders of Y<sub>2</sub>O<sub>3</sub>, ZrO<sub>2</sub>, and YSZ were used as starting materials. Cubic (bcc) Y<sub>2</sub>O<sub>3</sub> (yttrium(III) oxide, nanopowder, < 50 nm particle size) and tetragonal YSZ (zirconium(IV) oxide—yttria stabilized, nanopowder, containing 8 mol % Y<sub>2</sub>O<sub>3</sub> as stabilizer) were supplied by Sigma-Aldrich, and monoclinic ZrO<sub>2</sub> (with a small amount of tetragonal phase after thermal annealing at 1173 K, zirconium(IV) oxide, 99.978%) by Alfa Aesar. All samples were pretreated by calcination at 1173 K in air and subsequently checked by XRD for structural changes upon annealing (see Supporting Information Figure S4). The surface areas after the pretreatments were determined by nitrogen adsorption at 77 K according to the Brunner–Emmett–Teller (BET) method as 21.7 m<sup>2</sup> g<sup>−1</sup> (Y<sub>2</sub>O<sub>3</sub>), 31.6 m<sup>2</sup> g<sup>−1</sup> (YSZ), and 10.4 m<sup>2</sup> g<sup>−1</sup> (ZrO<sub>2</sub>). For BET measurements, a Quantachrome Nova 2000 Surface Area and Pore Size Analyzer was used. Methane was supplied by Messer (99.995%).

**2.2. Electrochemical Impedance Spectroscopy.** The electrical properties were investigated by electrochemical impedance spectroscopy. The impedance cell basically consists of an outer quartz tube with two inner quartz tubes, to which the electrodes are attached. Heating was provided by a tubular furnace and controlled by a

thermocouple (S-element), located in the reactor about 5 mm downstream of the sample, and a Micromega PID temperature controller. The impedance was measured by an IM6e impedance spectrometer (Zahner Messsysteme), which provides data on the impedance and the phase angle of the current as a function of voltage. For all measurements described in this article, a stimulation voltage of 20 mV and a low excitation frequency of 1 Hz were applied to two circular Pt electrodes. These form a plate capacitor in mechanically enforced contact with the sample pellet. For a typical experiment, the samples were heated up to 1173 K, held at 1173 K for 30 min, and subsequently, cooled down to 300 K at a rate of 10 K min<sup>−1</sup> in the respective gas atmosphere under flowing conditions (~1 mL s<sup>−1</sup>).

The electric impedance measurements were conducted under dry and moist conditions. To achieve dry conditions, a liquid N<sub>2</sub>–ethanol cooling trap at a temperature of approximately 143 K was used. To establish moist conditions (equilibrium vapor pressure of water at room temperature), distilled water was added to the cooling trap. A very similar experimental procedure to achieve dry and moist conditions also applies to the volumetric adsorption measurements (see section 2.3 and Supporting Information Figure S1). The difference in the procedure basically is that for the volumetric adsorption experiments only a small amount of water was added to the cooling trap, and freeze and thaw was performed several times to result in a reproducible water partial pressure of ~24 mbar.

**2.3. Volumetric Adsorption.** The volumetric adsorption measurements were conducted in an all-quartz apparatus equipped with metal bellow valves (Witeg), a Baratron pressure transducer (MKS), mass flow controllers (MKS), and a Balzers QMA125 quadrupole mass analyzer. The furnace was a Linn model capable of operation at up to 1500 K. Before each methane dissociation experiment and to ensure identical starting conditions, the samples were fully oxidized by heating in 1 bar of dry flowing O<sub>2</sub> to 1273 K. After heating at 1273 K for 1 h, the samples were cooled to 300 K in dry flowing O<sub>2</sub>, followed by evacuating the cell to about 5 × 10<sup>−7</sup> mbar. The volumetric adsorption experiments themselves involved heating from 313 K up to the final temperature of 1273 K at a linear rate of 10 K min<sup>−1</sup> in an initially static reaction mixture of CH<sub>4</sub> and Ar (1:1, 100 mbar each), maintaining the maximum temperature for 10 min, and then cooling to 300 K also at a rate of 10 K min<sup>−1</sup> (additional information on technical details is provided in Supporting Information Figure S1).

As the exact way of converting the raw mass spectrometry (MS) data into interpretable and comparable molar results is of paramount importance, at this stage, we provide a step-by-step discussion of converting the raw MS data into interpretable quantities. All samples were treated in a mixture of dry CH<sub>4</sub>:Ar (generally a ratio of 1:1 was used) to compensate the total pressure as well as the individual mass intensity readings for the loss of continuous gas withdrawal through the leak into the MS. Hence, the first step is always the correction of any raw MS signal and the pressure signal with the Ar signal. Subsequently, the next step is the conversion of the so-corrected intensity data into millibar values. The starting pressure of CH<sub>4</sub> (in mbar) is the reference for all further calculations, and the total amount of reaction- or adsorption consumed CH<sub>4</sub> can be easily recalculated for any stage of an experiment. The main goal of the measurement was to determine the amount of deposited carbon. The principally possible intermediate formation of ethylene and ethane, other small hydrocarbons, and C<sub>1</sub> oxygenates (via residual water) was neglected as the focus of this investigation was purely on C<sub>1</sub> conversion to solid carbon. The amount of deposited carbon was identified via a subsequent temperature-programmed oxidation (TPO) experiment. After the treatment of the sample in CH<sub>4</sub>/Ar, as described above, at first, a high vacuum was applied. Subsequently, an O<sub>2</sub>:Ar mixture (1:1 ratio) was introduced for “titration” of the deposited carbon by quantifying the total oxygen uptake from the decrease of the *m/z* = 32 MS signal. Due to the fact that only CO<sub>2</sub> formation was observed during the TPO experiments (but no CO, as verified by MS), the molar quantity of deposited carbon could be directly assigned to the equivalent molar oxygen uptake. Now, in the next step, it needs to be clarified if it is mainly the reaction CH<sub>4</sub> → C + 2H<sub>2</sub> that prevailed, in which case the

lion's share of converted  $\text{CH}_4$  and formed  $\text{H}_2$  can be assigned to almost equivalent molar amounts of C and  $2\text{H}_2$ . This was the case for all measurements with pure  $\text{Y}_2\text{O}_3$  and  $\text{ZrO}_2$  samples. In the case of YSZ, side reactions (with to-date not fully resolved relative contribution and chemistry) lead to an increased divergence between methane consumption and deposited amount of carbon. Provided that all side reactions were known, a full  $\text{C}_1$  mass balance would require a more complex calculation, which more or less would have to be based on the fraction of the total converted amount of  $\text{CH}_4$ , which was not deposited in the form of solid carbon. Also, the  $\text{H}_2$  mass balance must be influenced by these side reactions so that the exact stoichiometry of the  $\text{H}_2$  loss cannot be derived from our data. Thus, for the sake of simplicity, the simple stoichiometry  $\text{CH}_4 \rightarrow \text{C} + 2\text{H}_2$  was assumed to calculate the millibars of  $\text{H}_2$  formed. The precise molar value of hydrogen formation is, anyway, not important for qualitative illustration of the onset of carbon deposition, which is the central topic of this work. For better comparison also to literature-reported data, all mass spectrometer data (in mbar) were converted into micromoles on the basis of the ideal gas equation, with subsequent normalization to sample mass and surface area.

**2.4. Raman Spectroscopy.** Confocal Raman spectra of the polycrystalline samples in the range of  $50\text{--}3800\text{ cm}^{-1}$  were recorded with a Horiba Jobin Yvon Labram-HR 800 Raman micro spectrometer. The samples were excited using the  $532\text{ nm}$  ( $2.33\text{ eV}$ ) emission line of a frequency-doubled  $25\text{ mW}$  Nd:YAG laser under an Olympus  $100\times$  objective lens with a numerical aperture of  $0.9$ . The size of the laser spot on the surface was approximately  $1\text{ }\mu\text{m}$  in diameter. The scattered light was dispersed by an optical grating with  $1800\text{ lines mm}^{-1}$  and collected by a  $1024 \times 256$  open-electrode CCD detector. The spectral resolution, determined by measuring the Rayleigh line, was better than  $2\text{ cm}^{-1}$ . The spectra were recorded in unpolarized mode at ambient conditions. The accuracy of the Raman line shifts, calibrated by measuring a silicon standard, was in the order of  $0.5\text{ cm}^{-1}$ . First- and second-order polynomial and convoluted Gaussian–Lorentzian functions were fitted to background and Raman bands, respectively, using the built-in spectrometer software LabSpec 5.<sup>22</sup>

**2.5. TEM.** High-resolution imaging (HRTEM), electron-energy loss spectroscopy (EELS), and high-angle annular dark-field (HAADF) imaging were performed using a  $200\text{ kV}$  FEI TECNAI F20 S-TWIN analytical (scanning-) transmission electron microscope (S)TEM equipped with a Gatan GIF Tridiem and an aberration-corrected FEI Titan electron microscope operated at  $300\text{ kV}$ .

### 3. RESULTS AND DISCUSSION

#### 3.1. Electrochemical Impedance Spectroscopy.

**3.1.1. Dry Conditions.** Alternating current (AC) impedance analysis at  $1\text{ Hz}$  excitation frequency in the temperature range from  $300$  to  $1173\text{ K}$  was carried out for the  $\text{Y}_2\text{O}_3$ , YSZ, and  $\text{ZrO}_2$  samples to detect thermally induced changes in the conductivity, as well as potential charge-carrier-inducing stoichiometry changes (vacancy formation) during the treatment with methane. Prior to every impedance measurement, the samples were heated in dry flowing  $\text{O}_2$  ( $\sim 0.3\text{ mL s}^{-1}$ ) to  $1173\text{ K}$ . After heating at  $1173\text{ K}$  for  $30\text{ min}$ , the samples were cooled to  $300\text{ K}$ . The temperature-dependent impedance was subsequently measured as discussed in section 2.2.

Exposing the  $\text{Y}_2\text{O}_3$  sample to dry  $\text{CH}_4$  and heating it up to around  $1040\text{ K}$  (Figure 1A) results in semiconductive behavior with the reversible formation of thermally excited charge carriers, as can be deduced from the reversible impedance change between  $900$  and  $600\text{ K}$  (note that all values above  $3 \times 10^9\text{ }\Omega$  exceed the measurement range of the impedance spectrometer). However, a drastic decrease of the impedance, leading to a final value of around  $12\text{ }\Omega$ , is observed, starting at temperatures above  $1040\text{ K}$ . This value indicates the presence of a material with almost metallic conductivity, which—as will

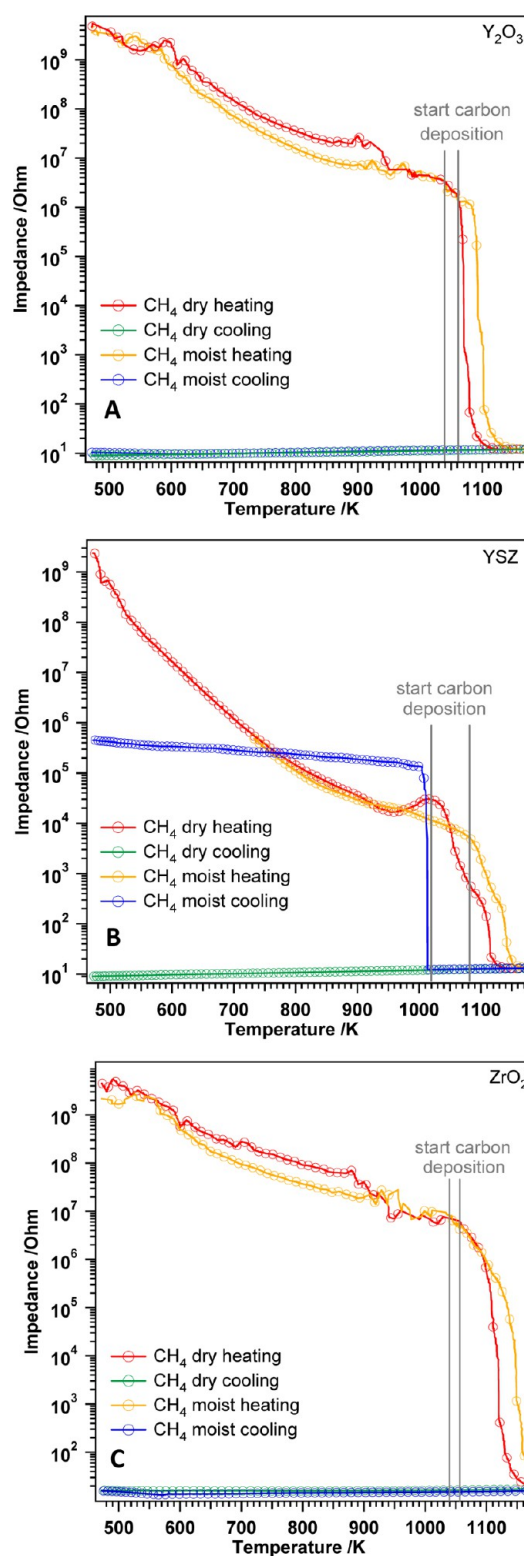


**Figure 1.** Electrochemical impedance spectroscopy measurements on  $\text{Y}_2\text{O}_3$  (A), YSZ (B), and  $\text{ZrO}_2$  (C) in dry and moist  $\text{CH}_4$  (flow  $\sim 0.7\text{ mL s}^{-1}$ ) at heating and cooling rates of  $10\text{ K min}^{-1}$  up to  $1173\text{ K}$  and back to  $300\text{ K}$ . An excitation signal of  $20\text{ mV}$  and a frequency of  $1\text{ Hz}$  were used.

be shown by Raman spectroscopy and electron microscopy in sections 3.3 and 3.4—is due to the presence of a conducting graphitic carbon layer formed by dissociation of methane. Even after recoiling to  $300\text{ K}$ , metallic conductivity is still preserved



(with a corresponding impedance value of  $\sim 9 \Omega$ ), implying that the carbon layer is still present on the  $\text{Y}_2\text{O}_3$  surface. The detailed features of the impedance decrease during heating with more or less discernible steps ( $\sim 900$ – $1100 \text{ K}$ ) possibly stems from reaction-induced changes of surface chemistry or from stepwise percolation of carbon islands to form more and more conducting graphite “channels”, leading to progressively increasing ohmic contribution to the impedance. A further increase of the temperature effectively leads to grain boundary polarization with a capacitive behavior. The higher the temperature, the more interconnected the deposited carbon layer becomes, finally leading to a conducting carbon layer with purely ohmic impedance.

Figure 1B shows the corresponding experiments in dry methane on the YSZ sample. Below  $\sim 950 \text{ K}$ , a similar semiconducting and reversible behavior as on  $\text{Y}_2\text{O}_3$  is observed. Of course, thermal excitability of charge carriers (predominantly  $\text{O}^{2-}$ ) is grossly increased relative to undoped  $\text{Y}_2\text{O}_3$  and  $\text{ZrO}_2$ . Upon further heating, a slight increase in the impedance is noticeable, with a maximum at  $1020 \text{ K}$  and a corresponding impedance value of  $2.9 \times 10^4 \Omega$ . Further raising the temperature up to a final value of  $1173 \text{ K}$  again leads to a decrease in the impedance with three noticeable steps: the first one takes place at  $1060 \text{ K}$  with a resulting impedance value of  $1.0 \times 10^3 \Omega$ , the second one at  $1115 \text{ K}$  with an impedance value of  $22 \Omega$ , and the third one at  $1125 \text{ K}$  (and  $15 \Omega$ ). At the end of the heating routine, a final value of  $13 \Omega$  was obtained. In close correlation to the experiments on  $\text{Y}_2\text{O}_3$ , recooling in dry methane to  $300 \text{ K}$  does not re-establish the high impedance as present before admission of methane. Rather, the unaltered high conductivity again points to a prevailing conducting carbon layer.

Finally, Figure 1C shows the impedance measurements on the corresponding  $\text{ZrO}_2$  sample in dry methane. In short, almost the same behavior as for the other two oxides was detected, with some temperature shift in the onset of the conductivity increase, including the irreversible formation of the conduction carbon layer. In all cases, the respective onset of carbon layer formation is indicated in Figure 1 by vertical lines as a rough guide to the eye.

**3.1.2. Moist Conditions.** A direct comparison between simple dry methane decomposition and methane “steam reforming related” conditions was attempted by performing the experiments of the previous section in the presence of water vapor. It has to be mentioned that the available water partial pressure of  $25 \text{ mbar}$  was strongly substoichiometric, but this substoichiometry was, anyway, a necessary prerequisite to obtain measurable carbon deposition at all. Such treatment of both the  $\text{Y}_2\text{O}_3$  and  $\text{ZrO}_2$  samples (Figure 1A and C) yields a very similar impedance vs temperature dependence, which in principle very much resembles that observed under dry conditions. This is true both for the semiconducting behavior at lower temperatures up to a temperature of  $1040 \text{ K}$  and the drastic impedance decrease finally leading to values in the low-ohm range at higher temperatures. One might, therefore, conclude that also under moist conditions, a similar conducting carbon layer is formed, which also persists upon cooling. The behavior of YSZ treated under similar experimental conditions is, however, different. Exposure of YSZ to moist methane causes no distinctive change in the impedance relative to dry conditions up to temperatures of  $\sim 1080 \text{ K}$ . At temperatures above  $1080 \text{ K}$ , the impedance decrease again exhibits three distinct steps at  $1130 \text{ K}$  ( $250 \Omega$ ), at  $1140 \text{ K}$  ( $36 \Omega$ ), and at

$1150 \text{ K}$  ( $16 \Omega$ ), leading to a final value of  $13 \Omega$ , comparable to what was observed under dry conditions. Formation of the aforementioned conducting carbon layer, therefore, is highly likely. In contrast, upon recooling, indeed a very distinctive change in the course of the impedance is observed. At  $\sim 1014 \text{ K}$  a steep impedance increase is observed, where the value of the impedance changes from  $12$  to  $1.3 \times 10^5 \Omega$ , followed by only a slight increase at even lower temperatures (to  $4.7 \times 10^5 \Omega$  at  $300 \text{ K}$ ). The results can only be consistently interpreted by an at least partial removal or detachment of the carbon layer, partially restoring the initial impedance and the semiconducting behavior of the oxide. This partial detachment can readily be seen in the corresponding TEM images (cf. Figure 9).

The complex interplay between the extent of the carbon layer (i.e., the annealing temperature) and the presence of water vapor is exemplified in Figure 2, highlighting that the

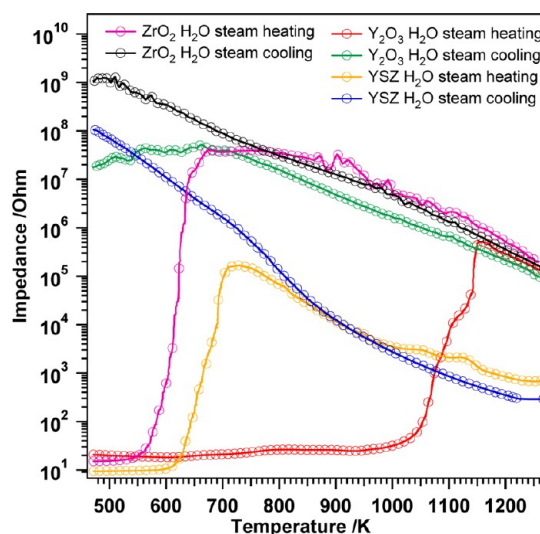


**Figure 2.** Electrochemical impedance spectroscopy measurements on  $\text{Y}_2\text{O}_3$ , YSZ, and  $\text{ZrO}_2$  after pretreatment in dry  $\text{CH}_4$  (flow  $\sim 0.7 \text{ mL s}^{-1}$ ) at a heating rate of  $10 \text{ K min}^{-1}$  up to  $1173 \text{ K}$  followed by a heating–cooling cycle in  $32 \text{ mbar H}_2\text{O}$  in He flow ( $\sim 0.4 \text{ mL s}^{-1}$ ) up to  $1273 \text{ K}$  using an excitation signal of  $20 \text{ mV}$  and a frequency of  $1 \text{ Hz}$ .

conducting carbon layer formed under dry conditions at  $1273 \text{ K}$  can be largely removed by treatment in  $\text{H}_2\text{O}$  vapor. For these experiments, water was added to the cooling trap and  $1 \text{ bar He}$  used as carrier gas with a flow of  $\sim 0.4 \text{ mL s}^{-1}$  through the apparatus. The resulting water partial pressure at  $300 \text{ K}$  amounted to  $\sim 32 \text{ mbar}$ .<sup>23</sup> Note that different onset temperatures of the  $\text{C-H}_2\text{O}$  reaction exist on all three oxides. For  $\text{ZrO}_2$  and YSZ, this steep onset is observed already at around  $600 \text{ K}$ ; for the  $\text{Y}_2\text{O}_3$ , it is shifted to  $1000 \text{ K}$ . Although a full, reactive clean-off reaction of carbon with water is indeed feasible at very high temperatures, the onset at lower temperatures (around  $600 \text{ K}$ ) is most likely associated with a partial detachment of the carbon layers, thus leading to an increased impedance.

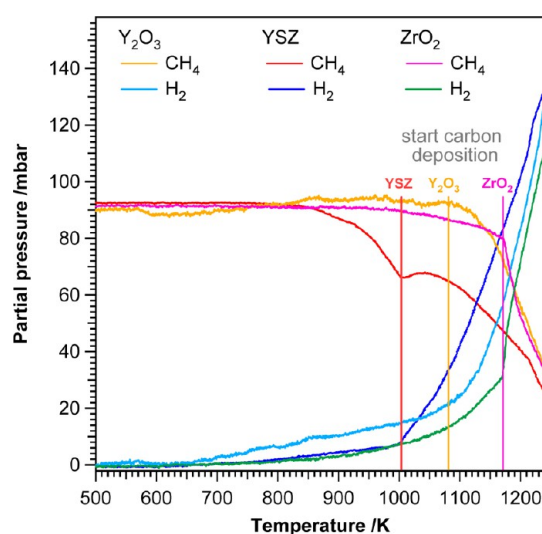
**3.2. Volumetric Adsorption.** From the above-discussed impedance results, an at least partial dissociation of methane, thereby depositing an up-to-now unknown amount of carbon on the oxide surface, can be deduced. Consequently, information about the degree of methane conversion as well as about the amount of deposited carbon material is highly desirable. To provide this information, volumetric adsorption

**Table 1.** Quantification of the Methane Dissociation and the Resulting Carbon Layer on  $\text{Y}_2\text{O}_3$ , YSZ, and  $\text{ZrO}_2$ 

	initial weight/g	$p(\text{CH}_4)$ decrease/mbar	deposited C/mbar	deposited C/ $\mu\text{mol g}^{-1}$	fraction not converted to carbon/mbar
$\text{Y}_2\text{O}_3$	0.0645	78	67	297.0	11
YSZ	0.2589	66	24	26.42	42
$\text{ZrO}_2$	0.5611	73	61	32.13	12

measurements have been performed in close correlation to the electric impedance measurements under different methane atmospheres. In-parallel monitoring of the methane and hydrogen traces (largely caused by the reaction  $\text{CH}_4 \rightarrow \text{C} + 2\text{H}_2$ ) yields information on both the onset of methane dissociation (i.e., if the methane dissociation occurs at similar temperatures as detected in the impedance measurements) and the exact amount of deposited carbon. The quantification details (methodology, in detail, is in the Experimental Section) are summarized in Table 1.

Figure 3 shows the comparative temperature-programmed reaction (TPR) experiments on all the oxides from 500 to 1273

**Figure 3.** Volumetric adsorption measurements on  $\text{Y}_2\text{O}_3$ , YSZ, and  $\text{ZrO}_2$  in dry  $\text{CH}_4$  up to 1273 K. Linear heating rate  $10 \text{ K min}^{-1}$ . The mass spectrometer signals of methane and hydrogen are shown.

K. On  $\text{Y}_2\text{O}_3$ , dissociative methane adsorption occurs at temperatures above 1080 K. This is both apparent from an uptake of methane by the sample and simultaneous production of hydrogen. Note that the steep decrease of methane above  $\sim 1100 \text{ K}$  exactly coincides not only with the accelerated rise of the hydrogen but also with the pronounced impedance drop discussed in Figure 1A at and above  $\sim 1000 \text{ K}$ . As shown in Table 1, a carbon layer with a total  $\text{C}_1$  amount of  $297 \mu\text{mol g}^{-1}$  (corresponding to 67 mbar methane) was formed on the surface of the  $\text{Y}_2\text{O}_3$  sample and 11 mbar of the methane (of a total methane decrease of 78 mbar) were not transformed to deposited carbon before the TPO measurement. A total of 86% of the converted amount of methane was, hence, directly transformed into deposited carbon material.

Temperature-programmed reactions over the YSZ sample in principle showed similar results. Partial methane conversion to a not fully resolved mix of products starts already at temperatures above 800 K. The main part of carbon deposition likely sets in at 1010 K, where, interestingly, a peculiar local minimum in the methane trace is visible, correlating with the beginning of the very steep slope of the  $\text{H}_2$  production curve

and with the bump in the impedance trace shown in Figure 1B. Why initially the methane dissociation is practically reversed remains unclear up to now. Because the experiments were performed in exactly the same manner as for  $\text{Y}_2\text{O}_3$  and  $\text{ZrO}_2$  (where this feature has never been observed), we might address this rather peculiar feature to an intrinsic property of YSZ. Note that also the corresponding methane “steam reforming” experiments using YSZ show exactly the same feature (Supporting Information Figure S2). As it exactly coincides with the increase in conductivity (cf. Figure 1, middle panel), we might also associate it with the removal of some part of the carbon layer at this temperature (note, however, that the drastic impedance drop only occurs at higher temperatures, finally leading to metallic conductivity). However, if either deposited carbon reacts to methane or, for example, intermediate ethane dissociates to subsequently form methane, these are in principle both hydrogen-consuming reactions. A strong increase of the hydrogen trace is therefore not anticipated, as long as no other hydrogen-releasing process (i.e., methane decomposition) is superimposed. Summarizing, we might assume that at least two different reactions with opposing trends in methane formation/decomposition are prevalent. In any case, more directed experiments to resolve the aforementioned side reactions are necessary to clarify this phenomenon. Table 1 shows, that according to the TPO analysis, a carbon layer of  $26 \mu\text{mol g}^{-1}$  (corresponding to 24 mbar) was deposited on the surface of the YSZ sample and 42 mbar of the methane (corresponding to 64% methane conversion) were not directly converted into deposited carbon material.

As shown in Figure 3, methane dissociation starts at slightly higher temperatures on  $\text{Y}_2\text{O}_3$ , but considerably more carbon is deposited on the sample surface as compared to YSZ. By comparing the impedance and volumetric adsorption curves, it is also evident that for up to 1040 K for  $\text{Y}_2\text{O}_3$  and 1000 K for YSZ, no significant methane consumption occurs, and the beginning of the methane dissociation is intimately connected with the sudden impedance drop above 1040 and 1000 K, respectively. This further confirms that methane dissociation predominantly leads to the formation of a conducting surface carbon layer on  $\text{Y}_2\text{O}_3$  and YSZ.

The measurements on  $\text{ZrO}_2$  very much resemble those of  $\text{Y}_2\text{O}_3$  and are also displayed in Figure 3. As shown in Table 1, a carbon layer with a total amount of  $32 \mu\text{mol g}^{-1}$  (corresponding to 61 mbar) was deposited on the surface of the  $\text{ZrO}_2$  sample and 12 mbar of the methane (with a total decrease of 73 mbar  $\text{CH}_4$ ) were not directly converted into deposited carbon material. The fraction of methane conversion into deposited carbon, hence, amounted to about 84%.

We also note that corresponding volumetric adsorption measurements have been conducted using a methane “steam reforming” mixture (30 mbar methane and 30 mbar argon, including 25 mbar water vapor; provided in the Supporting Information as Figure S2). As the relative contribution of “reforming” side reactions plus type is not known, quantification of the amount of deposited carbon is almost impossible. However, the general qualitative features resemble those

observed under dry conditions (cf. Figure 3), which also corroborates the above-discussed impedance measurements.

**3.3. Raman Spectroscopy.** In addition to electric impedance and volumetric adsorption studies, Raman measurements were performed to verify which kind of carbon material has been formed on the surface of the oxide samples. Raman spectroscopy is a particularly useful tool to provide qualitative analysis of carbon materials and to obtain information about other properties of the respective carbon species, such as their phonon and electronic structure or the presence of structural defects.<sup>24</sup> All Raman experiments were carried out at ambient conditions. To follow the kinetics of the formation of the carbon layers, Raman spectra of the samples treated at various temperatures have been collected.

**3.3.1. Dry conditions.** Nanocrystalline  $\text{Y}_2\text{O}_3$ , used as starting material, was exposed to  $\text{CH}_4$  and treated at 983, 1073, and 1173 K in methane (Figure 4A). Cubic  $\text{Y}_2\text{O}_3$  exhibits a dominant vibrational mode at  $377\text{ cm}^{-1}$  and additional bands at 138, 161, 197, 317, 377, 415, 452, 469, and  $585\text{ cm}^{-1}$ .<sup>25</sup> The Raman spectra of the specimens, annealed at 1073 and 1173 K, show additional bands due to the formation of carbon layers on the surface of the oxides. The prominent features are the nondispersive G-band (corresponds to double degenerate in-plane stretching vibrations of  $\text{sp}^2$ -bonded carbon atoms and is present around  $1550\text{--}1600\text{ cm}^{-1}$  in most graphite-like materials), the dispersive D-band (originates from structural disorder and is present around  $1340\text{--}1360\text{ cm}^{-1}$ ), the dispersive  $\text{G}'$ - or 2D-band (overtone or second-order harmonic of the D-peak which appears around  $2700\text{ cm}^{-1}$ ), and the combination mode of the G- and D-band (also due to structural disorder) around  $2950\text{ cm}^{-1}$ .<sup>26–29</sup> In the Raman spectrum of the specimen heated up to 1073 K, the G-peak is located at  $1599\text{ cm}^{-1}$ , the D-peak at  $1339\text{ cm}^{-1}$ , the  $\text{G}'$ -peak at  $2677\text{ cm}^{-1}$ , and the combination mode of the G- and D-peak at  $2929\text{ cm}^{-1}$ . The intensity ratio of the G- and D-peak indicates that the species formed on the  $\text{Y}_2\text{O}_3$  surface are most likely nanocrystalline graphite layers with a high degree of disorder. The Raman spectrum of the specimen heated to 1173 K shows the most distinctive peaks at around  $1596\text{ cm}^{-1}$  (G-peak),  $1341\text{ cm}^{-1}$  (D-peak),  $2677\text{ cm}^{-1}$  ( $\text{G}'$ -peak), and  $2929\text{ cm}^{-1}$  (combination mode of the G and D peak). Compared to the specimen heated to 1073 K, the ratio in the intensity of the G- and D-band has changed slightly, but nevertheless, it still indicates that highly disordered graphitic carbon is present.<sup>30–33</sup>

A similar analysis procedure was performed for YSZ (Figure 4B). The Raman spectrum of cubic YSZ is characterized by the fundamental optical modes at 149, 254, 316, 469, and  $635\text{ cm}^{-1}$ .<sup>34</sup> Although a treatment in methane at 973 K causes no changes with respect to the untreated sample, the Raman spectra of specimens heated to 1073 and 1173 K exhibit carbon-related vibrational modes. In case of the sample treated at 1073 K, these bands occur at 1339, 1600, 2680, and  $2929\text{ cm}^{-1}$ , though these modes can be observed at 1338, 1603, 2678, and  $2930\text{ cm}^{-1}$  for the 1173 K heat-treated specimen, respectively. As for  $\text{Y}_2\text{O}_3$ , the ratio between the G- and D-peak indicates nanocrystalline graphite with a high degree of disorder.

The Raman spectrum of pure  $\text{ZrO}_2$  shows external modes at 99, 179, 191,  $223\text{ cm}^{-1}$  and internal modes at 306, 334, 348, 382, 476, 503, 537, 559, 616, 639,  $758\text{ cm}^{-1}$  (compare with<sup>14</sup>). Exposure of the starting material to methane and heating up to 1073 and 1173 K results in similar frequencies of the G-, D-,

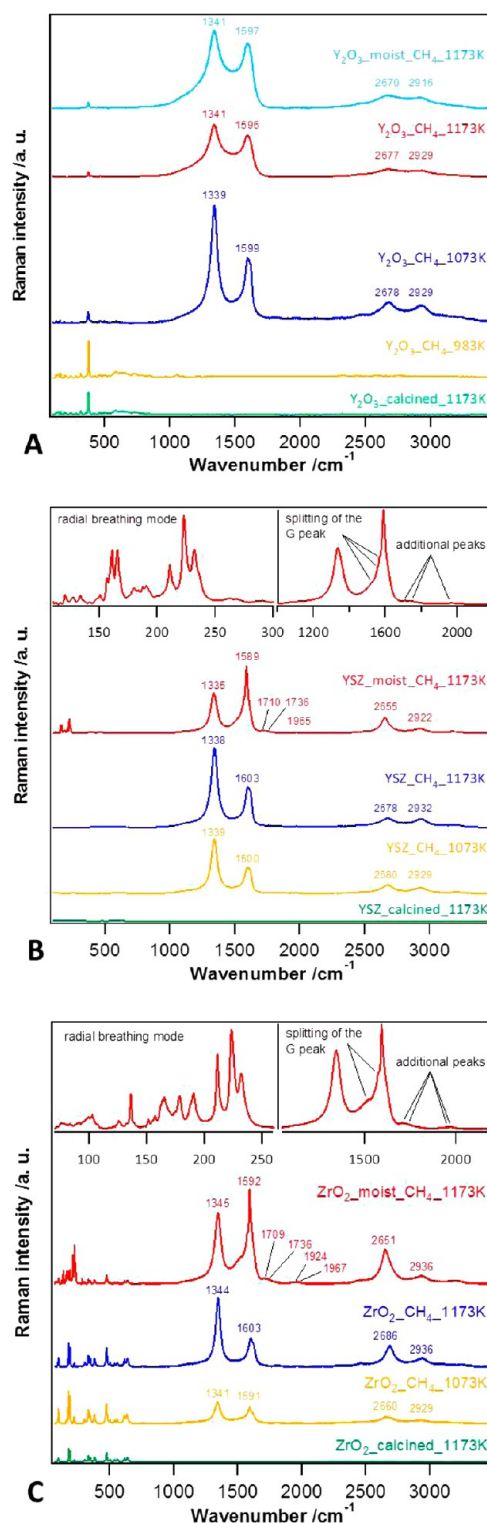


**Figure 4.** Selected Raman spectra on pure  $\text{Y}_2\text{O}_3$  (A), YSZ (B), and  $\text{ZrO}_2$  (C) after different annealing treatments (as indicated for the individual graphs) in air and after exposure to dry and moist methane. In panels B and C, enlargements in the upper left and upper right corner display the radial breathing modes and the G-peak splitting of the associated carbon nanotubes.

and  $\text{G}'$ -bands and combination modes of the G- and D-bands as for  $\text{Y}_2\text{O}_3$  and YSZ. Remarkable is the variation of the intensity ratio of the G- and D-peak between the two different heating temperatures. At 1073 K, the intensities of the G- and



D-peak have a ratio of 3:2, whereas at 1173 K the intensity of the D-peak is twice as high as the one of the G-peak. Nevertheless, the spectra still indicate the presence of nanocrystalline graphite sheets with a more or less high degree of disorder.

**3.3.2. Moist Conditions.** In the case of  $\text{Y}_2\text{O}_3$ , the frequencies of the Raman features do not substantially vary in comparison to the samples heated under dry conditions. Even the ratio of the intensity for the G- and D-peak is very similar. This further confirms that, in line with the impedance measurements, both in dry and moist methane structurally very similar carbon layers were formed on the surface of the three oxides, which can be clearly associated with highly disordered nanocrystalline graphite.

The Raman spectrum of YSZ heated up to 1173 K (Figure 4B) shows additional bands in comparison to the specimens treated under dry conditions, indicating the presence of a carbon nanotube-related material. The appearance of the so-called radial breathing mode (RBM) at low frequencies and the splitting of the G-band are characteristic features in the Raman spectrum of carbon nanotubes. The radial breathing mode is an out-of-plane phonon mode and corresponds to the coherent vibration of the carbon atoms in the radial direction, which generates an effect similar to “breathing”. The typical RBM range is from 100 to 350  $\text{cm}^{-1}$ . The G-peak shows two different components: the lower frequency component, which is associated with the confinement of the vibrational wave in the circumferential direction ( $\text{G}^-$ ), and the higher frequency component ( $\text{G}^+$ ), in correlation with vibrations along the direction of the nanotube axis. Furthermore, the intensity ratio of the G- and D-peak is generally used to determine the structural quality of carbon nanotubes. High-quality CNTs exhibit ratios considerably higher than 100.<sup>24</sup> The  $\text{G}'$ -peak feature is also present in the Raman spectra of CNT at around 2600  $\text{cm}^{-1}$ . It is an overtone or second-order harmonic of the D-peak, which is generated from a two-phonon, second-order scattering process that results in the creation of an inelastic phonon. Second-order modes are also apparent in the range between 1700–1800  $\text{cm}^{-1}$ .<sup>24</sup> These peaks are the so called  $\text{M}^-$  and  $\text{M}^+$  features, which are the overtones of the out-of-plane transversal optical mode (oTO) around 860  $\text{cm}^{-1}$ , which is infrared, but not Raman active. The Raman spectrum of YSZ (Fig. 4B), heat-treated up to 1173 K in moist  $\text{CH}_4$ , shows all the characteristic features of CNT's: the RBM between 100–350  $\text{cm}^{-1}$ , the D-peak at 1335  $\text{cm}^{-1}$ , and the G-peak at 1589  $\text{cm}^{-1}$ , which is split into several features. At 1710  $\text{cm}^{-1}$  ( $\text{M}^-$ ) and 1736  $\text{cm}^{-1}$  ( $\text{M}^+$ ), the overtones of the out-of-plane transversal optical (oTO) mode, and at 1965  $\text{cm}^{-1}$ , the combination mode of the iTO (in-plane transversal optical) mode and the LA (longitudinal acoustical) mode are clearly visible. Two high frequency peaks, assigned to the  $\text{G}'$ -peak at 2655  $\text{cm}^{-1}$  and the overtone of the LO (longitudinal optical) mode at around 2922  $\text{cm}^{-1}$ , are detected. The upper left inset in Figure 4B shows the radial breathing modes, caused by a bundle of carbon nanotubes, between 100–300  $\text{cm}^{-1}$ . The upper right inset plot clarifies the splitting of the G-peak and the additional peaks, which are due to the presence of carbon nanotubes.

In the same way, exposure of the  $\text{ZrO}_2$  sample to moist conditions and heating up to 1173 K also leads to the formation of carbon nanotubes (Figure 4C). The characteristic features such as the RBM between 100 and 350  $\text{cm}^{-1}$ , the D-peak at 1345  $\text{cm}^{-1}$ , and the G-peak at 1592  $\text{cm}^{-1}$ , which exhibits the

characteristic splitting, are all present. Also the overtones of the oTO mode are visible at 1709  $\text{cm}^{-1}$  ( $\text{M}^-$ ) and 1736  $\text{cm}^{-1}$  ( $\text{M}^+$ ) as well as the combination mode of the iTO mode and the LA at 1924 and 1967  $\text{cm}^{-1}$ , respectively. Additionally, the  $\text{G}'$ -peak at 2651  $\text{cm}^{-1}$  and the overtone of the LO at around 2936  $\text{cm}^{-1}$  occur in the Raman spectrum. In the upper left inset in Figure 4C, the radial breathing modes in the range between 50 and 260  $\text{cm}^{-1}$  are magnified. The upper right inset shows the splitting of the G-peak and the additional peaks that are due to the presence of CNTs.<sup>24,26,35,36</sup>

For further clarification, Figures 5 and 6 show comparisons of the D/G-band and RBM frequency regions on different

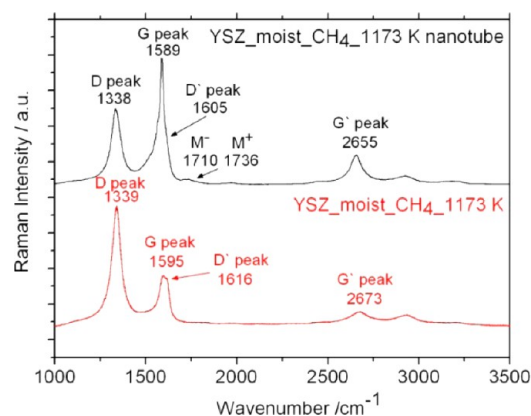


**Figure 5.** Raman spectra ( $\lambda_{\text{excitation}} = 532 \text{ nm}$ ) of YSZ after exposure to moist  $\text{CH}_4$  and heating up to 1173 K in the range of 1000–3500  $\text{cm}^{-1}$ . Variation of sample position has been performed in the micrometer range.

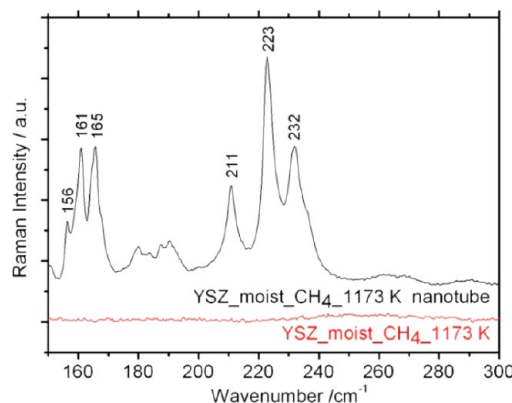


**Figure 6.** Raman spectra ( $\lambda_{\text{excitation}} = 532 \text{ nm}$ ) of YSZ after exposure to  $\text{CH}_4$  and heating up to 1173 K in the range of 150–300  $\text{cm}^{-1}$ . The upper Raman spectrum exhibits a range of modes in the region between 150 and 250  $\text{cm}^{-1}$ , which can be assigned to the radial breathing modes (RBM) of different nanotubes.

regions of the YSZ grains. As it is clear from these results, the formation of the carbon nanotubes is not a common feature but occurs only in certain regions of the YSZ grains. The overwhelming majority of the sample only shows peaks associated with distorted crystalline graphite. This assumption is corroborated by the TEM images shown, which clearly show that the carbon nanotubes are formed via local, partial detachment of these graphite layers, in turn also giving rise to the increased impedance upon cooling as shown in Figure 1B (blue trace).

The upper (black) Raman spectrum shows a splitting of the so-called G mode and additional vibrational modes as compared with the lower (red) Raman spectrum. These additional features are characteristic for carbon nanotubes. Furthermore, the D peak of the lower Raman spectrum exhibits a higher intensity as compared to the G peak, indicating a higher structural disorder of the carbon material.

**3.4. TEM.** To finally make the carbon layer visible, (aberration-corrected) electron microscopy measurements were conducted before and after exposure of the samples to methane. Figure 7A exemplifies a representative agglomerate of intimately connected  $\text{Y}_2\text{O}_3$  grains with two sets of atomically resolved (222) lattice spacing of the bcc  $\text{Y}_2\text{O}_3$  structure. The atoms at the particle edges are well resolved and clearly, no covering overlayer is present. After exposure to dry  $\text{CH}_4$  at 1173 K (Figure 7B), no distinct changes in the morphology of the  $\text{Y}_2\text{O}_3$  grains are observed, but clearly, the grains are covered by at least one carbon layer. Between two and five individual layers with the characteristic layer distance of the graphite sheets (3.3 Å) are visible (note the line profile shown as the inset; this is the typical spacing in all relevant HRTEM images). Figure 7C additionally shows a high-resolution detail of a rosette-like carbon species (marked with a white arrow) and the highly distorted, almost amorphous carbon layer (marked with a black arrow). Note that none of these species has been observed on the pure, untreated  $\text{Y}_2\text{O}_3$  sample. Hence, the presence of the conducting carbon layer is finally also revealed directly by an imaging technique. In Figure 8, a representative image of a YSZ particle after  $\text{CH}_4$  treatment is highlighted. Clearly, also in this case, a carbon layer covering the individual YSZ grains is visible. C–K EEL spectra taken at the spot of the carbon layer (indicated by the white arrow) show the characteristic peak shapes of the  $\pi^*$  and  $\sigma^*$  features of disordered graphite.<sup>37</sup> Furthermore, the TEM images can be used to give a rough estimate about the amount of carbon deposited, in close correlation to the volumetric adsorption experiments. Assuming an average number of individual graphene sheets of four, the total number of carbon atoms in these four layers can be estimated from the atom number density of individual carbon atoms within a single graphene layer. From the lattice constant  $a = 142 \text{ pm}$  ( $1.42 \times 10^{-10} \text{ m}$ ), the atom number density  $\eta$  can be calculated via  $\eta = (N/A) = (4/9)(\sqrt{3}/a^2)$  (with  $A$  as the area of a hexagon and  $A = 6(a^2/4)\sqrt{3}$ ) to  $3.18 \times 10^{19}$  carbon atoms per square meter of a single layer. The total number of carbon atoms in four layers, thus, amounts to  $1.52 \times 10^{20}$  atoms. Conversion into mol carbon yields  $3.04 \times 10^{-4} \text{ mol}$  and, assuming an initial weight of  $0.0645 \text{ g}$  and a surface area of  $21.7 \text{ m}^2 \text{ g}^{-1}$  (for  $\text{Y}_2\text{O}_3$ ),  $470 \mu\text{mol g}^{-1}$  deposited carbon. This basically confirms the amount deduced from the volumetric adsorption measurements ( $\sim 300 \mu\text{mol g}^{-1}$ ).

Figure 9 shows TEM images taken after treating the  $\text{Y}_2\text{O}_3$  (panels A and B) and YSZ (panels C and D) samples under moist conditions. In close correlation with the electric impedance and Raman measurements, the detached carbon layers are clearly visible, in turn giving rise to a higher impedance and Raman features similar to those of carbon nanotube-like materials. Note that these detached carbon layers are exclusively formed upon treatment under moist conditions.

**3.5. Discussion.** As the growth of different carbon nanoarchitectures is of great technological interest, studies on catalyst-assisted transformation of hydrocarbons into carbon nanostructures, especially graphene, graphitic materials, and

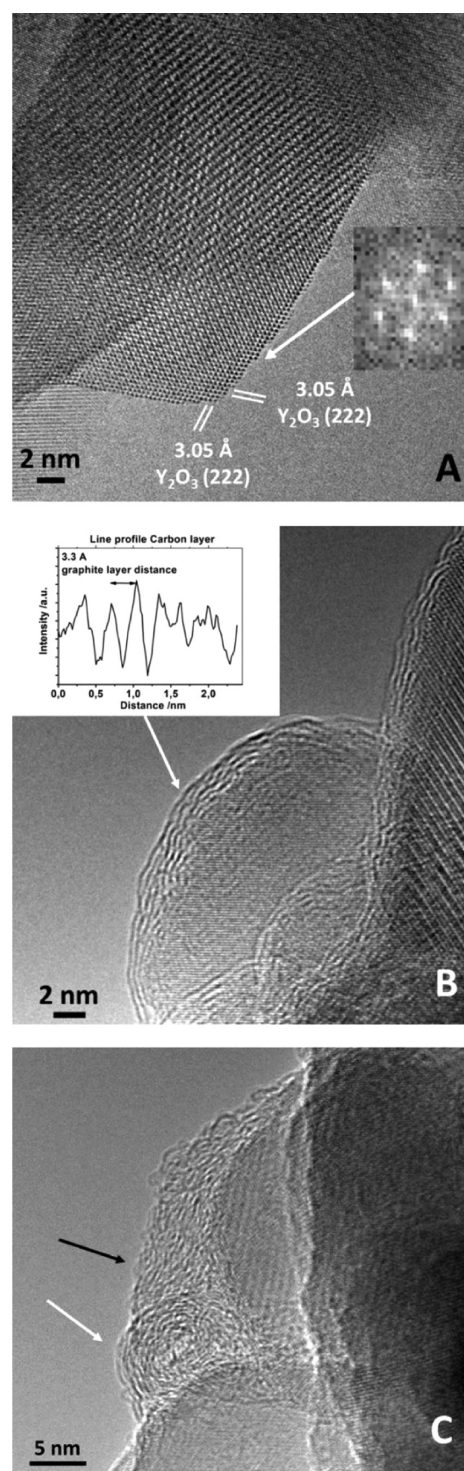


**Figure 7.** HRTEM image of pure  $\text{Y}_2\text{O}_3$ , calcined up to 1173 K (A) and after exposure to dry methane at 973 K (B and C). The inset in panel B shows the line profile of the carbon atom layer distances covering the individual  $\text{Y}_2\text{O}_3$  grains.

single- and multiwalled carbon nanotubes are abundant.<sup>32,38–43</sup> Without reviewing the state-of-the-art in detail, one important piece of information that appears to be still partly missing is the question about the formation mechanism, especially those of carbon nanotubes, on oxide surfaces. It is now widely accepted that not only metallic substrates may act as potentially active catalysts but also carbide and oxide materials may be used as



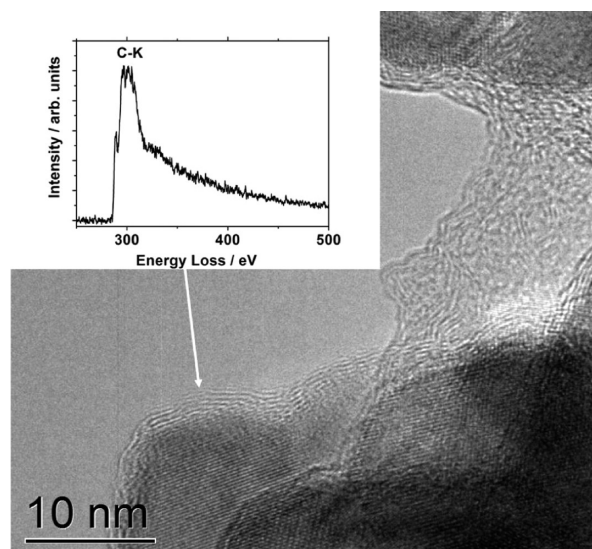


**Figure 8.** HRTEM image of a pure YSZ particle after exposure to dry methane at 1073 K. The inset highlights an C–K EEL spectrum taken at the spot of the carbon layer, revealing the characteristic peak shape of structurally distorted graphite.

growth templates. However, especially on the latter, the formation mechanism is still subject to a matter of discussion, and the role of the experimental parameters (such as the presence of water vapor) and the oxide's reducibility are controversially discussed. In the case of alumina, non-stoichiometric  $\text{AlO}_x$  has been reported to aid the water-assisted carbon growth following dissociation of acetylene.<sup>44</sup> Nevertheless, it has also been shown that substoichiometric  $\text{AlO}_x$  (as well as fully oxidized  $\text{Al}_2\text{O}_3$ ) does not exhibit a capability for direct acetylene dissociation.<sup>45</sup> In line with these results,  $\text{ZrO}_2$  has been shown to act as an efficient catalyst for CNT growth and graphitization of amorphous carbon. During carbon growth, no reduction of  $\text{ZrO}_2$  to metallic Zr or carbothermic reduction to  $\text{ZrC}$  has been observed, but a potential beneficial role of substoichiometric  $\text{ZrO}_x$  species has been hypothesized.<sup>15</sup> Introduction of defects, therefore, were thought to play a role in the catalytic action of nanoparticulate  $\text{ZrO}_2$ .<sup>15</sup>

In this context, it has to be mentioned that methane conversion over differently doped oxide catalysts via gas phase radical chemistry is by no means a novel concept—a huge amount of catalytic literature is available on the well-studied topic of methane oxidative coupling toward ethane and ethene<sup>46</sup> as well as that of thermal methane decomposition to yield hydrogen and carbon without forming carbon oxides as

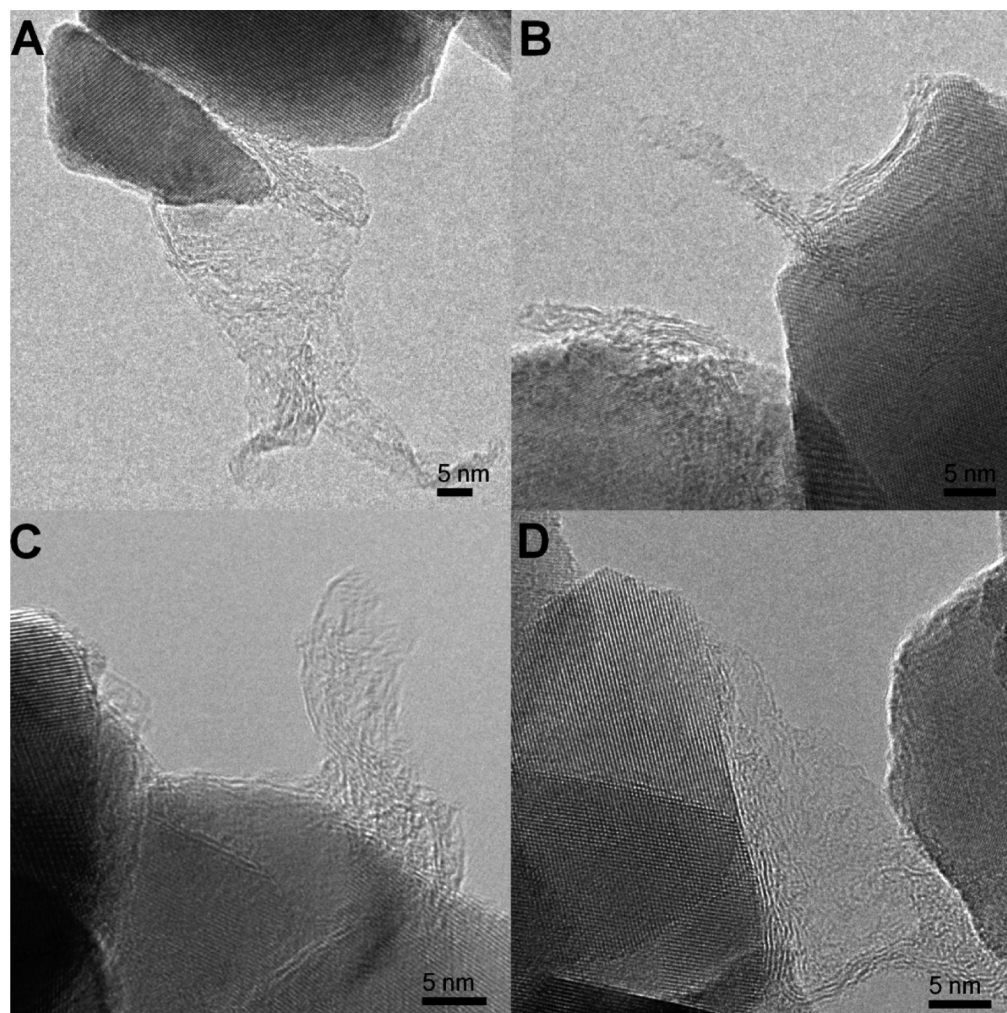


**Figure 9.** HRTEM images of particles after exposure to moist methane at 1073 K. Panels A and B show detached carbon layers on  $\text{Y}_2\text{O}_3$ ; panels C and D show those on YSZ.

unwanted byproducts.<sup>47,48</sup> The general features of high-temperature methane gas phase chemistry, even in the absence of any catalyst surface, are well-known.<sup>47,48</sup> Methane thermolysis to form methyl radicals starts, even in the absence of any catalytic surface, at  $T \geq 1000$  K. The subsequent reaction steps toward  $C_2$  molecules involve processes of coupling of methyl radicals to ethane and hydrogen strip-off reaction from ethyl radicals to form ethene.<sup>47</sup> Once molecules like ethene and acetylene are formed, these will start to condense into monocyclic and polycyclic aromatic moieties at sufficiently high temperatures. Depending on the catalyst, even a high selectivity to benzene can be achieved.<sup>49</sup> The role of the catalytic (oxide) surface is to interact with the individual gas phase intermediates in a directional manner toward a desired product; thus, thermal methane conversion at temperatures above 1000 K can be viewed as a combination of a homogeneous radical gas phase reaction mechanism with selectivity-steering surface-related “heterogeneous” reactions.<sup>50</sup> In oxidative coupling, the role of the substoichiometric  $O_2$  gas phase component is to remove unwanted carbon deposits from the surface and to force the reaction thermodynamically versus methane dehydrogenation to yield  $C_2$  moieties, that is, to withdraw the formed hydrogen from the gas phase in the form of water. Naturally, in the complete absence of oxygen, and if insufficient water vapor for the “full” methane reforming stoichiometry is available, all methane must finally end up as a carbon deposit. What is new in the recent literature on carbon growth on oxides,<sup>15</sup> and thus also in the present study, is a more detailed look at the specific carbon architectures that grow under strongly reducing conditions on variable oxide surfaces and, in this work, particularly on SOFC-relevant oxide surfaces, where unwanted coking is a major issue with respect to the desired internal reforming and direct electro-oxidation of methane and other hydrocarbon fuels. Consequently, it must be assumed that the universally observed initial “homogeneous–heterogeneous” reaction mechanism proceeding via  $C_2$  intermediates is also the key to the detailed growth mechanism of the observed variable carbon structures on a broad range of oxide surfaces.

Putting our results into perspective, we note that it is, thus, not too surprising that all three oxides exhibit the capability of direct methane activation, which has been verified by a range of complementary structural and spectroscopic characterization methods. According to the electric impedance measurements, no substantial reduction of any of the oxides, but only the reversible formation of thermally excited charge carriers at lower annealing temperatures, takes place, and the strong impedance drop at  $T \geq 1000$  K is solely due to the buildup of a conducting carbon layer. Selected area electron diffraction patterns also do not indicate the formation of substoichiometric phases, which is anyway not expected under the given experimental conditions. Neither  $ZrO_2$  nor  $Y_2O_3$  are subject to reduction by  $H_2$  at 1773 K and higher,<sup>51</sup> and also carbothermic reduction does not take place (at least for  $ZrO_2$ ) below 1473 K,<sup>52</sup> that is, both at temperatures much higher than used in this work. Reduction studies of YSZ are nonexistent, but as the overall shape of the experiments are similar to  $Y_2O_3$  and  $ZrO_2$ , we rather suspect that, also in this case, substantial reduction does not occur. As the carbon diffusion in bulk  $ZrO_2$ ,<sup>15</sup>  $Y_2O_3$ , and YSZ is low (given also the successful growth of a carbon ad-layer around the oxide grains), we infer a combined gas-phase-surface-controlled growth mechanism, the exact role of which needs to be clarified in

detail on the basis of a detailed analysis of the particular gas phase and surface intermediates preceding carbon growth. A special focus should be directed on the basicity of the respective oxide surfaces because this has been shown to be the most important parameter for, for example, methane coupling activity.<sup>46</sup>

A potentially important parameter (which also has been shown to crucially influence the adsorption of CO and  $CO_2$ ,<sup>53</sup>) with respect to the cohesive stability and, even more, the adhesion of the grown (or just growing) carbon is very likely the hydroxylation degree of the respective oxide surfaces. Chemically bonded water will certainly play an important role also in the detailed growth morphology of the carbon architectures and their transformation. The ability to bind water depends on the individual oxide chemistry and for the studied oxides, the hydrophilicity, as well as the basicity, decreases in the order  $Y_2O_3 > YSZ > ZrO_2$ , especially given the high-temperature calcination treatment before the actual measurements.<sup>53</sup>  $Y_2O_3$ , therefore, is rather hygroscopic and efficient dehydroxylation is hardly possible.  $ZrO_2$ , on the other hand, once dehydroxylated, essentially remains in a dehydroxylated state, but YSZ rather shows the features of a “diluted”  $Y_2O_3$  chemistry.<sup>53</sup> In this respect, we note that the growth of carbon nanotube-like material on our oxide samples has exclusively been observed under moist conditions, implying a complex interplay between surface hydroxyl groups and adsorbed (or just forming) polyaromatic carbon species. As observed in the TEM images shown in Figure 9, detachment of the carbon films is much more pronounced if the samples are treated under moist conditions. This detachment of graphitic sheets gives rise to the spectroscopic fingerprints in the Raman spectrum that are associated to nanotube-like structures. We, therefore, conclude that the formation of the nanotube-like features is not due to direct catalytic influence of the oxide itself but is predominantly steered by the enhanced hydroxylation degree of the surface when treated under moist conditions. This is also corroborated by recent studies on other oxides, such as alumina (where the so-called water-assisted “super-growth” mode has been observed, leading to efficient CNT growth within seconds<sup>15</sup>). Efficient “localized” carbon deposition to initiate CNT growth, therefore, seems to require a delicate balance between the carbon deposition rate from the hydrocarbon feedstock, water adsorption to the appropriate degree of hydroxylation, and hydrogen, which also has been shown to influence the growth mode of carbon species. In our case, this would refer to the presence of both surface hydroxyl groups and water vapor in the reaction mixture, whereby especially the former is almost impossible to control quantitatively. Corroborating the suggested importance of these hydroxyl groups, Figure 2 reveals how sensitive the formed carbon layer to the presence of hydroxyl groups is and that a deposited carbon layer can be very easily detached or “de-percolated” at lower temperatures by deliberate admission of water already at temperatures of  $\sim 600$  K.

#### 4. CONCLUSIONS

From the results, we conclude that the presented oxides, among many others, indeed may act as efficient substrates for methane-induced carbon deposition. A set of experimental parameters exist that allows formation of different carbon species, including disordered graphite layers and, by surface dehydroxylation, also carbon nanotube-like material. As the temperature region where methane dissociation occurs coincides with the operating



conditions of solid oxide fuel cells, we infer also implications for the use of especially YSZ as electrolyte material. Coke formation during direct internal reforming of hydrocarbons and the associated carbon filament formation and eventual electrode fracture is one of the central and most important problems in fuel cell research. Although it is usually discussed only for Ni-cermet electrodes, with Ni particles being particularly active for carbon deposition, we show that hydrocarbon activation under conventional fuel cell operation is not limited to the metal component or the metal/oxide system. Rather, the contribution of the oxide electrolyte may not be neglected. This is especially important because it is suspected that the triple-phase boundary of anode/electrolyte/fuel is the center of the catalytic activity of any fuel cell. Therefore, the actions of each of the components have to be accurately known to understand the propensity of the triple-phase interface to coking. Further research will be directed at a thorough understanding of the corresponding metal-oxide systems treated under similar experimental conditions, that is, how the introduction of the metal component affects the methane activation capability of the pure oxide and how extensive coking can eventually be substantially suppressed.

## ■ ASSOCIATED CONTENT

### ■ Supporting Information

Figure S1: Schematic depiction of the volumetric adsorption apparatus. Figure S2: Volumetric adsorption measurement of YSZ in moist CH<sub>4</sub>. Figure S3: XRD patterns of the calcined oxide samples and the samples treated under dry methane up to 1173 K. This information is available free of charge via the Internet at <http://pubs.acs.org>.

## ■ AUTHOR INFORMATION

### Corresponding Author

\*S. Penner. E-mail: [simon.penner@uibk.ac.at](mailto:simon.penner@uibk.ac.at). Tel.: 00 43 512 5075 8003. Fax: 00 43 512 507 2925.

### Notes

The authors declare no competing financial interest.

## ■ ACKNOWLEDGMENTS

We thank the FWF (Austrian Science Foundation) for financial support under the project F4503-N16.

## ■ REFERENCES

- (1) Fenech, J.; Viazzi, C.; Ansart, F.; Bonino, J. P. *Thermec 2009 Supplement: 6th International Conference on Processing & Manufacturing of Advanced Materials* **2010**, 89–91, 184–189.
- (2) Jung, W.; Hertz, J. L.; Tuller, H. L. *Acta Mater.* **2009**, 57 (5), 1399–1404.
- (3) Fonseca, F. C.; de Florio, D. Z.; Muccillo, R. *Solid State Ionics* **2009**, 180 (11–13), 822–826.
- (4) Lee, B. K.; Lee, J. Y.; Jung, H. Y.; Lee, J. H.; Hwang, J. H. *Solid State Ionics* **2008**, 179 (21–26), 955–959.
- (5) Talebi, T.; Sarrafi, M. H.; Haji, M.; Raissi, B.; Maghsoudipour, A. *Int. J. Hydrogen Energy* **2010**, 35 (17), 9440–9447.
- (6) Kim, S.; Kwon, O.; Kumar, S.; Xiong, Y.; Lee, C. *Surf. Coat. Technol.* **2008**, 202 (14), 3180–3186.
- (7) Cho, H. J.; Choi, G. M. *J. Power Sources* **2008**, 176 (1), 96–101.
- (8) Li, T. S.; Wang, W. G.; Miao, H.; Chen, T.; Xu, C. *J. Alloys Compd.* **2010**, 495 (1), 138–143.
- (9) Kim, S. D.; Moon, H.; Hyun, S. H.; Moon, J.; Kim, J.; Lee, H. W. *Solid State Ionics* **2006**, 177 (9–10), 931–938.
- (10) Macek, J.; Novosel, B.; Marinsek, M. *J. Eur. Ceram. Soc.* **2007**, 27 (2–3), 487–491.
- (11) Lanzini, A.; Leone, P.; Guerra, C.; Smeacetto, F.; Brandon, N. P.; Santarelli, M. *Chem. Eng. J.* **2013**, 220, 254–263.
- (12) Marinsek, M. *Bol. Soc. Esp. Ceram. Vidrio* **2011**, 50 (3), 135–142.
- (13) You, H.; Gao, H.; Chen, G.; Abudula, A.; Ding, X. *J. Power Sources* **2011**, 196 (5), 2779–2784.
- (14) You, J. L.; Jiang, G. C.; Yang, S. H.; Ma, J. C.; Xu, K. D. *Chin. Phys. Lett.* **2001**, 18 (7), 991–993.
- (15) Steiner, S. A., III; Baumann, T. F.; Bayer, B. C.; Blume, R.; Worsley, M. A.; MoberlyChan, W. J.; Shaw, E. L.; Schloegl, R.; Hart, A. J.; Hofmann, S.; Wardle, B. L., Nanoscale Zirconia as a Nonmetallic Catalyst for Graphitization of Carbon and Growth of Single- and Multiwall Carbon Nanotubes. *J. Am. Chem. Soc.* **2009**, 131 (34).
- (16) Hata, K.; Futaba, D. N.; Mizuno, K.; Namai, T.; Yumura, M.; Iijima, S. *Science* **2004**, 306 (5700), 1362–1364.
- (17) Teblum, E.; Gofer, Y.; Pint, C. L.; Nessim, G. D. *J. Phys. Chem. C* **2012**, 116 (46), 24522–24528.
- (18) Amama, P. B.; Pint, C. L.; Mirri, F.; Pasquali, M.; Hauge, R. H.; Maruyama, B. *Carbon* **2012**, 50 (7), 2396–2406.
- (19) Pint, C. L.; Pheasant, S. T.; Parra-Vasquez, A. N. G.; Horton, C.; Xu, Y.; Hauge, R. H. *J. Phys. Chem. C* **2009**, 113 (10), 4125–4133.
- (20) Eres, G.; Kinkhabwala, A. A.; Cui, H. T.; Geohegan, D. B.; Puzos, A. A.; Lowndes, D. H. *J. Phys. Chem. B* **2005**, 109 (35), 16684–16694.
- (21) Chakrabarti, S.; Nagasaka, T.; Yoshikawa, Y.; Pan, L.; Nakayama, Y. *Jpn. J. Appl. Phys., Part 2* **2006**, 45 (24–28), L720–L722.
- (22) LABSPEC S. Horiba Scientific: Longjumeau Cedex, France, 2010.
- (23) Onken, U.; Rarey-Nies, J.; Gmehling, J. *Int. J. Thermophys.* **1989**, 10 (3), 739–747.
- (24) Dresselhaus, M. S.; Dresselhaus, G.; Saito, R.; Jorio, A. *Phys. Rep.* **2004**, 409 (2), 47–99.
- (25) Wang, L.; Pan, Y.; Ding, Y.; Yang, W.; Mao, W. L.; Sinogeikin, S. V.; Meng, Y.; Shen, G.; Mao, H.-K. *Appl. Phys. Lett.* **2009**, 94 (6), 061921.
- (26) Lehman, J. H.; Terrones, M.; Mansfield, E.; Hurst, K. E.; Meunier, V. *Carbon* **2011**, 49 (8), 2581–2602.
- (27) Reich, S.; Thomsen, C.; Maultzsch, J. *Carbon Nanotubes*; Wiley VCH: Weinheim, Germany, 2004.
- (28) ICBME 2008—13th International Conference on Biomedical Engineering; Lim, C.; Goh, J., Eds.; Springer: New York, 2008; Vol. 23.
- (29) Pimenta, M. A.; Dresselhaus, G.; Dresselhaus, M. S.; Cancado, L. G.; Jorio, A.; Saito, R. *Phys. Chem. Chem. Phys.* **2007**, 9 (11), 1276–1291.
- (30) Praver, S.; Ninio, F.; Bianchonette, L. *J. Appl. Phys.* **1990**, 68, 2361.
- (31) Vitali, G.; Rossi, M.; Terranova, M. L.; Sessa, V. *J. Appl. Phys.* **1995**, 77 (9), 4307–4311.
- (32) McEvoy, N.; Peltekis, N.; Kumar, S.; Rezvani, E.; Nolan, H.; Keeley, G. P.; Blau, W. J.; Duesberg, G. S. *Carbon* **2012**, 50 (3), 1216–1226.
- (33) Lopez-Honorato, E.; Meadows, P. J.; Shatwell, R. A.; Xiao, P. *Carbon* **2010**, 48 (3), 881–890.
- (34) Naumenko, A. P.; Berezovska, N. I.; Biliy, M. M.; Shevchenko, O. V. *Vibrational Analysis and Raman Spectra of Tetragonal Zirconia. Phys. Chem. Solid State*; **2008**; Vol. 9, pp 121–125.
- (35) Costa, S.; Borowiak-Palen, E.; Kruszynska, M.; Bachmatiuk, A.; Kalenczuk, R. J. *Mater. Sci.—Pol.* **2008**, 26 (2), 433–441.
- (36) Lei, X.-W.; Ni, Q.-Q.; Shi, J.-X.; Natsuki, T. *Nanoscale Res. Lett.* **2011**, 6, 492.
- (37) Ahn, C. C.; Krivanek, O. L. *EELS Atlas*; Gatan: Pleasanton, CA, 1983.
- (38) Bourdain, V.; Bichara, C. *Carbon* **2013**, 58, 2–39.
- (39) Shaikjee, A.; Coville, N. J. *Carbon* **2012**, 50 (10), 3376–3398.
- (40) Gohier, A.; Ewels, C. P.; Minea, T. M.; Djouadi, M. A. *Carbon* **2008**, 46 (10), 1331–1338.
- (41) Xiao, N.; Zhou, Y.; Ling, Z.; Qiu, J. *Carbon* **2013**, 59, 530–536.
- (42) Cui, C.; Qian, W.; Zheng, C.; Liu, Y.; Yun, S.; Yu, Y.; Nie, J.; Wei, F. *Chem. Eng. J.* **2013**, 223, 617–622.



- (43) Kuan, C.-F.; Kuan, H.-C.; Ma, C.-C. M.; Chen, C.-H.; Wu, H.-L. *Mater. Lett.* **2007**, *61* (13), 2744–2748.
- (44) Noda, S.; Hasegawa, K.; Sugime, H.; Kakehi, K.; Zhang, Z.; Maruyama, S.; Yamaguchi, Y. *Jpn. J. Appl. Phys., Part 2* **2007**, *46* (17–19), L399–L401.
- (45) Mattevi, C.; Hofmann, S.; Cantoro, M.; Ferrari, A. C.; Robertson, J.; Castellarin-Cudia, C.; Dolafi, S.; Goldoni, A.; Cepek, C. *Phys. E (Amsterdam, Neth.)* **2008**, *40* (7), 2238–2242.
- (46) Zavyalova, U.; Holena, M.; Schlögl, R.; Baerns, M. *ChemCatChem* **2011**, *3*, 1935–1947.
- (47) Chen, C.-J.; Back, M. H.; Back, R. A. *Can. J. Chem.* **1975**, *53*, 3580–3590.
- (48) Chen, C.-J.; Back, M. H.; Back, R. A. *Can. J. Chem.* **1976**, *54*, 3175–3184.
- (49) Solymosi, F.; Szöke, A.; Cserenyi, J. *Catal. Lett.* **1996**, *39*, 157–161.
- (50) Lunsford, J. H. *Catal. Today* **2000**, *63*, 165–174.
- (51) McTaggart, F. K. *Nature* **1961**, *191*, 1192.
- (52) Sacks, M. D.; Wang, C. A.; Yang, Z. H.; Jain, A. *J. Mater. Sci.* **2004**, *39* (19), 6057–6066.
- (53) Koeck, E.-M.; Kogler, M.; Biele, T.; Kloetzer, B.; Penner, S. *J. Phys. Chem. C* **2013**, *117* (34), 17666–17673.